

Coupling 1D stellar evolution with 3D-hydrodynamical simulations on-the-fly II: Stellar Evolution and Asteroseismic Applications

Jakob Rørsted Mosumgaard^{1,2*}, Andreas Christ Sølvesten Jørgensen,^{2 †} Achim Weiss²,
V́ctor Silva Aguirre¹ and Jørgen Christensen-Dalsgaard^{1,3}

¹ *Stellar Astrophysics Centre (SAC), Department of Physics and Astronomy, Aarhus University, Ny Munkegade 120, DK-8000 Aarhus C, Denmark*

² *Max-Planck-Institut für Astrophysik, Karl-Schwarzschild-Str. 1, D-85748 Garching, Germany*

³ *Kavli Institute for Theoretical Physics, University of California Santa Barbara, CA 93106-4030*

Accepted 2019 October 21. Received 2019 October 13; in original form 2019 July 7

ABSTRACT

Models of stellar structure and evolution are an indispensable tool in astrophysics, yet they are known to incorrectly reproduce the outer convective layers of stars. In the first paper of this series, we presented a novel procedure to include the mean structure of 3D hydrodynamical simulations on-the-fly in stellar models, and found it to significantly improve the outer stratification and oscillation frequencies of a standard solar model. In the present work, we extend the analysis of the method; specifically how the transition point between envelope and interior affects the models. We confirm the versatility of our method by successfully repeating the entire procedure for a different grid of 3D hydro-simulations. Furthermore, the applicability of the procedure was investigated across the HR diagram and an accuracy comparable to the solar case was found. Moreover, we explored the implications on stellar evolution and find that the red-giant branch is shifted about 40 K to higher effective temperatures. Finally, we present for the first time an asteroseismic analysis based on stellar models fully utilising the stratification of 3D simulations on-the-fly. These new models significantly reduce the asteroseismic surface term for the two selected stars in the *Kepler* field. We extend the analysis to red giants and characterise the shape of the surface effect in this regime. Lastly, we stress that the interpolation required by our method would benefit from new 3D simulations, resulting in a finer sampling of the grid.

Key words: asteroseismology – stars: atmospheres – stars: evolution – stars: interiors – stars: oscillations – stars: solar-type

1 INTRODUCTION

An essential part of stellar structure calculations is the description of convection: the hydrodynamical phenomenon when energy cannot be transported stably by radiation alone. One of the most successful approaches from an astrophysical point of view is the mixing-length theory (MLT), which is an approximative, parametric description of convection. The basic principle is to model convection as rising and falling elements moving a certain distance in a stable background medium before dissolving. As described by e.g. Gough & Weiss (1976), the mixing-length approach to convection was developed in the early 20th century by several independent authors. The MLT was applied in an astronomical context by Biermann (1932), and introduced to stellar modelling in a generalised form by Böhm-

Vitense (Vitense 1953; Böhm-Vitense 1958), whose formalism has since been the most common one.

The advantage of utilizing such parametrizations is that the nuclear reactions – rather than the convection motion – set the time scale for the evolution calculations. A drawback of the MLT approach is that it involves free parameters, several of which are specified by the employed MLT flavour (e.g. Böhm-Vitense 1958; Cox & Giuli 1968; Kippenhahn et al. 2012). However, the most important one – the so-called mixing-length parameter α_{MLT} – must be determined from a calibration, which is typically performed to reproduce the Sun (e.g. Gough & Weiss 1976; Pedersen et al. 1990; Salaris & Cassisi 2008).

The MLT description of convection is known to be inadequate (e.g., Trampedach 2010) and results in incorrectly modelled outer layers in low-mass stars with convective envelopes (e.g., Rosenthal et al. 1999). This gives rise to a systematic offset in the predicted oscillation frequencies, which was observed in the Sun, and confirmed by helioseismology to stem from near-surface deficiencies in

* E-mail: jakob@phys.au.dk

† E-mail: acsj@mpa-garching.mpg.de

the stellar models (Brown 1984; Christensen-Dalsgaard & Gough 1984; Christensen-Dalsgaard et al. 1988). Today, it is commonly referred to as the (asteroseismic) *surface effect*, and it is crucial to take it into consideration when using oscillation frequencies to determine stellar parameters. In the context of helioseismic inversions, the surface term is typically suppressed by introducing a constraint based on a series of polynomials (e.g. the review by Christensen-Dalsgaard 2002, and references therein). In asteroseismology, a correction in the form of an empirical prescription is commonly used; two of the most popular ones are the power law by Kjeldsen et al. (2008), and the prescription by Ball & Gizon (2014).

To improve the modelling of the outer structure, an option is to utilise 2D or 3D radiation-coupled hydrodynamics simulations of stellar surface convection. These simulations require no parametric theory; the convection is generated from fundamental physics by treating the interaction between radiation and matter. Such 3D simulations are inherently more realistic and have altered our understanding of solar granulation and stellar convection (e.g. Stein & Nordlund (1989, 1998); Nordlund et al. 2009).

The first attempts to include information from such simulations to adjust models of the present Sun were made by Schlattl et al. (1997) and Rosenthal et al. (1999). Recently, several authors (Piau et al. 2014; Sonoi et al. 2015; Ball et al. 2016; Magic & Weiss 2016; Trampedach et al. 2017) have produced stellar models, where the outer layers of the 1D structure are substituted by the mean stratification of 3D simulations. This procedure is commonly referred to as patching, and requires a high degree of physical consistency between the two model parts. It also requires a careful fit of the 1D model to the 3D counterpart to ensure that the fundamental stellar surface parameters of the two match. Due to the high computational cost of hydrodynamical simulations, these methods are based on pre-calculated 3D atmospheres/envelopes.

A major limitation of these patching procedures is that they have limited applicability: They can only be used to analyse a star with parameters exactly matching those of a computed simulation. In order to circumvent this, Jørgensen et al. (2017) – hereafter J17 – established a new method to interpolate between 3D simulations in atmospheric parameters (effective temperature, T_{eff} , and surface gravity, $\log g$). The scheme was able to reliably reproduce the mean structure of 3D envelopes from two existing sets of simulations: The Stagger grid (Magic et al. 2013) and the grid from Trampedach et al. (2013). Currently, only interpolation between simulations at solar metallicity – as defined in the respective 3D-simulation grids – are supported. J17 was able to construct patched models for stars not matching any existing 3D simulations – including several stars observed by the *Kepler* space mission (Borucki et al. 2010; Gilliland et al. 2010).

An inherent drawback of the patching methods – which is not remedied by the J17-interpolation – is that they do not take information from 3D simulations into account *during* the entire evolution. Only at the final model the outer layers are substituted; the evolution prior to this point is calculated using a stellar evolution code using a standard α_{MLT} -prescription and analytical boundary condition.

In order to overcome this shortcoming, Trampedach et al. (2014a,b) took another path to including 3D information in stellar models. Utilizing the hydro-grid from Trampedach et al. (2013), they distilled each simulation into a stratification of temperature T as a function of optical depth τ – a so-called $T(\tau)$ relation, which can be used as a boundary condition in a stellar model – capable of reproducing the 3D photospheric transition. They also performed a corresponding calibration of α_{MLT} , which can be used by stel-

lar evolution codes throughout the evolution (for stars inside the simulation grid). How stellar evolution is affected by employing this parametrisation was initially investigated by Salaris & Cassisi (2015) and Mosumgaard et al. (2017). Recently, Mosumgaard et al. (2018) published details on how to implement the results in a stellar evolution code, and presented an in-depth analysis of the structural and asteroseismic impact, which turns out to be quite limited.

In the first paper of this series, Jørgensen et al. (2018) – hereafter Paper I – presented a novel method for using averaged 3D-envelopes on-the-fly for stellar evolution. The ⟨3D⟩-envelopes are both used as boundary conditions to determine the interior structure and are appended in each iteration of the calculation – thus omitting the need for post-evolutionary patching. The analysis showed that our new method leads to a calibrated solar model, whose outer layers closely mimic the structure of the underlying 3D simulations. Moreover, this improvement of the stellar structure is shown to partly eliminate the structural contribution to the surface effect.

In the present work, we extend the investigation of using ⟨3D⟩-envelope on-the-fly for stellar evolution. We elaborate upon aspects not treated in Paper I as well as extend the analysis to stars of different parameters. We defer interpolation in metallicity on-the-fly to a later paper. A scheme for interpolation in metallicity was recently presented by Jørgensen et al. (2019) but has not yet been implemented into a stellar evolution code. In the current paper we neglect turbulent pressure; however, an implementation of this was recently presented by Jørgensen & Weiss (2019).

The paper is organised as follows. In the next section, the method is briefly summarised, and in Section 3 we investigate further aspects of the solar model. We apply our procedure to a different grid of 3D simulations in Section 3.3. The impact on stellar evolution and structure models is examined in Section 4. In Section 5, we analyse the asteroseismic impact of our new models and extend the discussion to red giants in Section 6. Our concluding remarks are found in Section 7.

2 METHOD

In this section, we briefly summarize key aspects of our method. For further details on the implementation, we refer to Paper I.

Our calculations are made with the Garching Stellar Evolution Code (GARSTEC, Weiss & Schlattl 2008) combined with a grid of 3D hydro-simulations of stellar surface convection. In this paper – except for in Section 3.3 – we use simulations from the Stagger grid by Magic et al. (2013) at solar metallicity.

We have employed the interpolation scheme from J17 – using the current T_{eff} and $\log g$ of the star – to determine an interpolated mean stratification. The fundamental quantity of the procedure is the gas pressure as a function of temperature $P_{\text{gas}}(T)$ extracted from the full 3D simulations. Note that the shallowest 3D simulation in the grid dictates the highest possible pressure in the interpolated envelope (see J17).¹

The obtained ⟨3D⟩-envelope is used to provide the outer boundary conditions for solving the stellar structure equations in the stellar

¹ When determining the interpolation range, it is important to exclude the un-physical border regions that strongly reflect the chosen lower boundary conditions. We have excluded these zones based on the superadiabatic index: $\nabla - \nabla_{\text{ad}}$, where $\nabla = d \ln T / d \ln P$. Rather than approaching adiabatic conditions, this quantity increases with depth in the un-physical regime.

model. In our implementation, the boundary conditions are established deep within the superadiabatic layer – we refer to the corresponding point in the model as the *matching point* (see next section). In other words, this matching point is the outermost point in the interior part and the innermost point in the envelope.

As the photosphere is not a part of the interior model, the first step is to infer the current T_{eff} by other means. We do this by setting up another interpolation in the Stagger grid, this time based on matching point temperature T_m . By assuming the interior and envelope parts to have a common temperature at the matching point, the T_{eff} corresponding to this T_m can be evaluated from the interpolation. With T_{eff} established, we interpolate in the Stagger grid to obtain the gas pressure as a function of temperature – in practice a scaled pressure is used (discussed below). Then the gas pressure at the bottom of the envelope is compared to the corresponding value predicted by the interior model for its outer mesh point – this is our boundary condition. Thus, in the converged model the gas pressure of the outermost point in the interior matches the value at the innermost point of the envelope – of course the temperature also matches by construction.

Outside the matching point we directly adopt $P_{\text{gas}}(T)$ from the interpolated ⟨3D⟩-envelopes – we refer to this part of the combined model as the *appended envelope*. Here the density ρ and the first adiabatic index Γ_1 are computed from the equation of state (EOS) used in the stellar evolution code. The radius r and mass $M(r)$ at each mesh point in the envelope are calculated from hydrostatic equilibrium, and the photospheric radius of the star is determined based on T_{eff} and Stefan-Boltzmann’s law.

In all of our models we use the OPAL opacities (Iglesias & Rogers 1996) extended with the low-temperature opacities from Ferguson et al. (2005). To be consistent with the simulations in the Stagger grid we use the Asplund et al. (AGSS09, 2009) solar composition. For the calculations, we employ the FreeEOS by A. W. Irwin² (Cassisi et al. 2003).

2.1 The matching point

An important feature in the stratification of the 3D simulations is the minimum in $\partial \log \rho / \partial \log P_{\text{gas}}$, which was called the *density jump* in the nomenclature of J17 and Paper I. Given the nature of this near-surface feature, the term *density inflection (point)* might be more accurate; however, to avoid the confusion of modifying the nomenclature, we keep the label *jump* in the following. The pressure and density at this point can be used to construct the *scaled pressure* and *scaled density*, which are the foundation of our method. The logarithm of these quantities are shown for the simulations at solar metallicity from the Stagger grid in Fig. 1, where the density feature is also marked.

As introduced in Paper I, the matching point between interior and appended ⟨3D⟩-envelope is selected at a fixed scaled pressure. We introduce the quantity

$$K_m = \log_{10} \left(\frac{P_{\text{gas}}}{P_{\text{jump}}} \right)_{\text{matching point}}, \quad (1)$$

i.e., the value of the logarithm of the scaled pressure at the matching point is dubbed K_m . Our typical choice is $K_m = 1.20$ – which is near the right dotted line in Fig. 1 – such that the pressure at the matching point is $10^{1.20} \approx 15.8$ times higher than the pressure at the density feature near the surface. The exact choice determines the

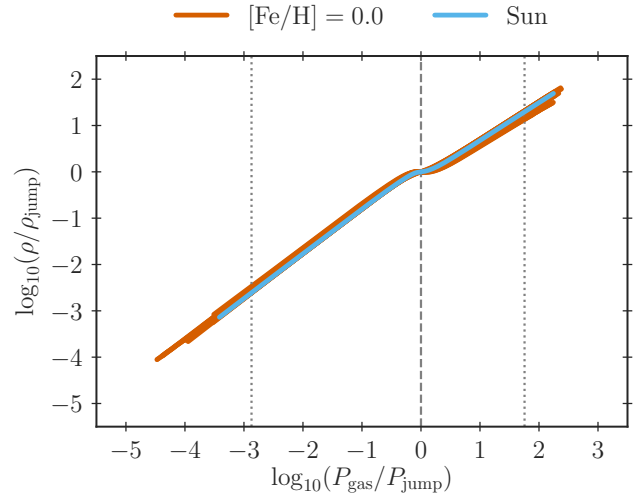


Figure 1. Scaled density stratification as a function of the scaled pressure for all 28 Stagger-grid simulations at solar metallicity. The stratification of the solar simulation is overlaid. The dotted lines mark the interpolation range. The dashed line highlights the density inflection point, the so-called density jump (details in text). For the equivalent plot, including all 199 relaxed simulations from the Stagger grid, we refer to Jørgensen et al. (2019, Fig. 1).

depth and will influence the produced model, which we will explore in Section 3.2.

3 SOLAR MODELS

In Paper I we performed a solar calibration with our new implementation to obtain a standard solar model (SSM) with ⟨3D⟩-envelopes appended on-the-fly in the evolution. In the following we will expand the discussion of the solar structure and evolution, and address several aspects not treated in Paper I.

3.1 The equation of state

As mentioned above, temperature and pressure are taken directly from the interpolated ⟨3D⟩-envelope in the appended part of the model, while we rely on the EOS from GARSTEC to supply the remaining quantities. Paper I showed that the density is recovered to very high accuracy. Another important quantity – which we will investigate in the following – is the first adiabatic index $\Gamma_1 = (\partial \ln P_{\text{gas}} / \partial \ln \rho)_{\text{ad}}$, which is not reproduced as accurately and thus might affect the asteroseismic result.

We utilize the same solar calibration as described in Paper I (Sec. 3), i.e., one calibrated to yield $T_{\text{eff}} = 5769$ K matching the Stagger grid solar simulation. The ⟨3D⟩-envelopes were used in the entire evolution. The matching point was at $K_m = 1.20$ (see eq. (1)) during the entire calculation, and the obtained mixing-length parameter is $\alpha_{\text{MLT}} = 3.30$. Note that a direct comparison between the mixing length used here and the standard mixing length used to characterize the superadiabatic region in normal MLT is not meaningful. In the present case, the role of the mixing-length parameter is to calibrate a tiny bit of superadiabaticity below the matching region, and hence it is very sensitive to the matching point and the details of the simulations. Thus, the actual numerical value

² <http://freeeos.sourceforge.net/>

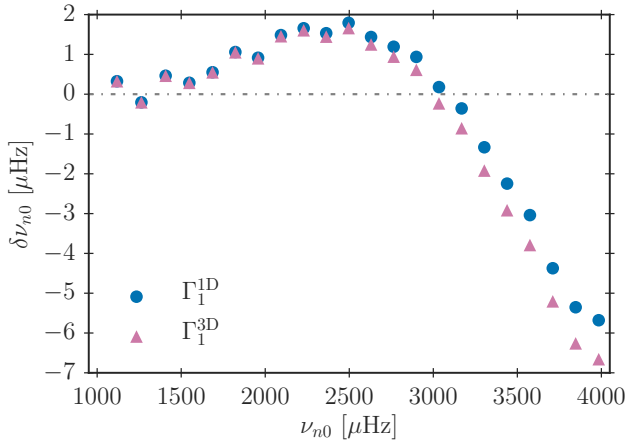


Figure 2. Frequency difference, $\delta\nu_{n\ell}$, between radial modes ($\ell = 0$) from model predictions and BiSON data. The predictions are from the solar calibrated model from Paper I using either Γ_1 from GARSTEC’s EOS (Γ_1^{1D}) or directly from the interpolated (3D)-envelope (Γ_1^{3D}).

of α_{MLT} are not important and in particular not relevant for any other model.

The predicted stellar oscillation frequencies, $\nu_{n\ell}$, are calculated with the Aarhus adiabatic oscillation package (ADIPLS, Christensen-Dalsgaard 2008). As discussed by Paper I, Γ_1 can be used directly in the frequency computation because we (currently) neglect turbulent pressure in our models constructed on-the-fly (Rosenthal et al. 1999; Houdek et al. 2017). In order to assess the impact of using the adiabatic index from the EOS, we substitute the value computed by GARSTEC, Γ_1^{1D} , with the values taken directly from the interpolated (3D)-envelope, Γ_1^{3D} , in our calibrated solar model. We then recompute the oscillations, again using Γ_1 directly. As we are fully neglecting turbulent pressure, the different “ Γ_1 cases” from Rosenthal et al. (1999) is not relevant.

The comparison is shown in Fig. 2, as frequency differences compared to observations from Birmingham Solar Oscillation Network (BiSON, Broomhall et al. 2009; Davies et al. 2014). To keep the comparison simple and to not clutter the plot only radial modes ($\ell = 0$) are shown. As can be seen from the figure, the effect is very small; the impact on the frequencies is around 1 μHz at the highest frequencies, and even less at the frequency of maximum oscillation power, $\nu_{\text{max}} \simeq 3100 \mu\text{Hz}$, and below.

3.2 The matching depth

The choice of matching point (introduced in Section 2.1) determines the depth of the appended envelope and affects the parameters of the solar calibration. In the following we perform ten different solar calibrations – computed to match a standard solar $T_{\text{eff}} = 5779 \text{ K}$ instead of the Stagger one – with different matching points in order to investigate to which extent the matching point affects the obtained structure, evolution, and seismic results. The different calibrations are denominated by the K_m from eq. (1).

The selected matching point given by the scaled pressure is used in the entire solar calibration routine, i.e., for the full evolution and not just in the final solar model. This fixed scaled pressure of the matching point is by construction constant throughout the evolution; however, for any given model in the sequence, the radius coordinate r_m of the matching point – valid only for that particular

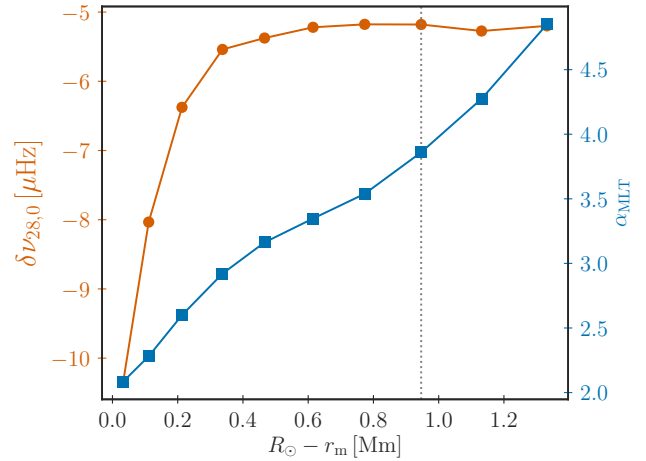


Figure 3. Results from the solar calibrations as a function of matching depth below the surface of the solar model. *Left ordinate (orange circles):* Difference between BiSON data and model frequencies for the $\ell = 0, n = 28$ mode. *Right ordinate (blue squares):* The calibrated mixing length α_{MLT} . The vertical dashed line marks the depth that correspond to $K_m = 1.20$, i.e., the scaled pressure at the matching point in Section 3.1. The conversion to K_m for several depths is presented in Fig. 4 and its caption.

model – can be reported as well. For the final resulting solar model this conversion can ease the discussion and especially in terms of physical matching depth below the surface $d_m = R - r_m$.

Firstly, we analyse the stellar oscillations for each of the ten solar models. Below a matching depth of $d_m \approx 0.6 \text{ Mm}$ – which roughly corresponds to the minimum in Γ_1 near the surface – we find the computed model frequency differences to be virtually depth independent. Furthermore, when the matching point is placed close to the surface, the obtained frequencies are very similar to those obtained with a standard Eddington grey atmosphere. The difference between the predicted model frequency and BiSON data for the $n = 28$ radial oscillation mode – corresponding to roughly 4000 μHz – is shown in orange in Fig. 3 as a function of matching depth for all of the different solar models.

Secondly, we investigate the mixing length parameter α_{MLT} , which is an output of the solar calibration. In order to correctly reproduce the solar surface properties, higher values of α_{MLT} are required when matching deeper below the surface (i.e. at a higher scaled pressure). The corresponding values for each matching depth are shown in blue in Fig. 3, from which it is clear that α_{MLT} is found to monotonically increase with increasing r_m . A similar result was obtained by Schlattl et al. (1997), when appending mean structures of 2D envelope models. Also note that the calibration with the same matching depth as used in the previous section and Paper I ($K_m = 1.20$) does not yield the same mixing-length parameter, due to the different target T_{eff} . The 10 K difference changes the value from $\alpha_{\text{MLT}} = 3.30$ to $\alpha_{\text{MLT}} = 3.86$.

The influence of the matching point on the model’s evolution is worth investigating – especially since the matching depth significantly alters the calibrated value of α_{MLT} . Therefore we calculated the evolution – continuing up the red-giant branch (RGB) – of the solar calibrated models. The resulting tracks for half of the cases (to not clutter the plot) are shown in Fig. 4. In the plot, the tracks are denoted by K_m , which is kept fixed for the entire evolution, and shown alongside the simulations from the Stagger grid used to obtain the interpolated (3D)-envelope appended on-the-fly.

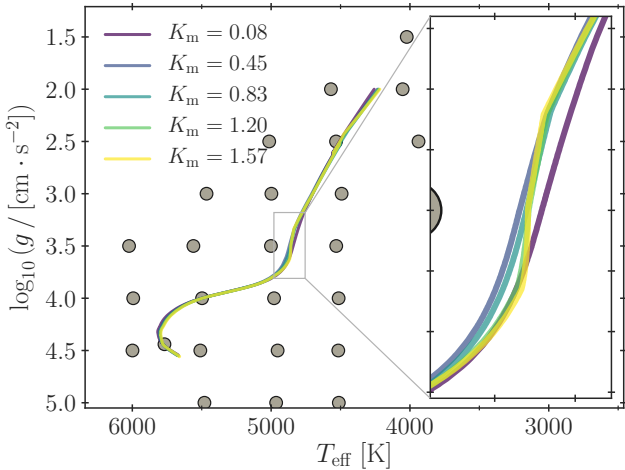


Figure 4. Evolution of the solar calibration models from the main sequence to the RGB. The ticks on the zoomed inset correspond to 100 K and 0.1 dex, respectively. The grey dots marks the Stagger grid models at solar metallicity. The tracks are denoted by K_m – a larger value implies a larger matching depth. For the present Sun, the listed scaled pressures correspond to a depth of 0.11 Mm, 0.34 Mm, 0.61 Mm, 0.95 Mm and 1.33 Mm, respectively (see Fig. 3).

From the figure it can be seen that the matching depth slightly alters the position of the turn-off as well as the temperature evolution on the RGB, but the effects are tiny. A more pronounced feature is the emerging kink at the bottom of the RGB – clearly visible from the zoom-in in Fig. 4 – which we suspect to be a result of the interpolation. As discussed briefly earlier and more extensively in Paper I, we compute the effective temperature T_{eff} of our models from interpolation in $\log g$ and the temperature at the matching point T_m (in Paper I referred to as T_m^{3D}). While the Stagger grid is almost regular in the $(T_{\text{eff}}, \log g)$ -plane, this is not the case in the $(T_m, \log g)$ -plane, due to the non-linear relationship between T_{eff} and T_m . This effect is shown in Appendix A for $K_m = 1.20$. Moreover, as the matching depth is changed, the simulation points move individually in this parameter space, which causes the separation between them to change.

The result is that the larger the matching depth gets, the lower the resolution in some regions of the $(T_m, \log g)$ -plane is, which implies a higher risk for interpolation errors in the determined T_{eff} . As can be seen from Fig. 4, the evolutionary tracks show kinks on the RGB that become more pronounced with increasing matching depth. Based on this, our method would strongly benefit from a refinement of the Stagger grid; specifically a few additional 3D simulations with $\log g = 3.0 - 4.0$ and $T_{\text{eff}} = 4500 - 5000$ K. We expand on the discussion of interpolation and grid resolution in Section 4.1.

In order to fully take advantage of the 3D simulations, it is generally desirable to place the matching point as deep within the nearly adiabatic region as possible. As just mentioned, problems can however emerge in the post-main sequence evolution if the matching is performed near the bottom of the simulations. Thus, deciding on the matching depth is a compromise between these two considerations. Until further 3D simulations are calculated, an intermediate matching depth in the nearly adiabatic region is preferable – such as the depth used in Section 3.1 (identical to Paper I) and in the following sections, corresponding to $K_m = 1.20$.

3.3 The Trampedach grid

To investigate the versatility of our method, we have repeated the analysis of the solar model from Paper I with a different set of 3D simulations: The grid from Trampedach et al. (2013) consisting of 37 simulations at solar metallicity.³ In this section, the interpolated $\langle 3D \rangle$ -envelopes are determined from the simulations in this grid.

For consistency, we calculate our models with the same non-canonical solar mixture as this set of 3D simulations employs (Trampedach et al. 2013, Table 1) – in which $Z/X = 0.0245$ – as well as the specific atmospheric opacities from Trampedach et al. (2014a,b) provided by R. Trampedach (priv. comm.). The low-temperature opacities are merged with interior opacities from the Opacity Project (OP, Badnell et al. 2005) for the same, identical composition.

The procedure for setting up the boundary conditions and appending the $\langle 3D \rangle$ -envelopes on-the-fly is identical to what is described in Section 2 and Paper I. In the nomenclature of earlier sections, the scaled pressure at the matching point corresponds to $K_m = 0.88$. For the present Sun, the pressure at the matching point corresponds to a temperature of $T_m = 1.29 \times 10^4$ K and a depth of $d_m = 0.64$ Mm below the photosphere. The appended envelope is hence shallower than the envelope of the solar calibration model using the Stagger grid presented by Paper I.

For comparison, we calculated a solar calibration with identical input physics, but using a standard Eddington grey atmosphere – labelled *Edd.* in the plots and table of this section. Moreover, the use of the grid from Trampedach et al. (2013) and compatible input physics allows us to compare our method to the work by Mosumgaard et al. (2018), which is a different approach for using information from 3D simulation in stellar evolution models. In this procedure – which also relies on interpolation in T_{eff} and $\log g$ – the outer boundary conditions are supplied by $T(\tau)$ relations extracted from the 3D simulations by Trampedach et al. (2014a), and the models include a variable 3D-calibrated α_{MLT} from Trampedach et al. (2014b). This specific solar model is taken from Mosumgaard et al. (2018) and is denoted *RT2014* in the following.

The resulting parameters from the three different calibrations are shown in Table 1. As found in Paper I, our change in the outer boundary conditions does not affect the surface helium mass fraction Y_s nor the radius of the base of the convection zone r_{CZ} . For comparison, the results from helioseismology are: $Y_s = 0.2485 \pm 0.0035$ (Basu & Antia 2004) and $r_{\text{CZ}} = 0.713 \pm 0.001 R_{\odot}$ (Basu & Antia 1997). Regarding the mixing-length parameter, we find the same as before and refer to the earlier discussion: that a direct comparison of the two cases is not meaningful and that the actual values of α_{MLT} are not important.

A comparison of the temperature structure of the resulting solar models and the 3D solar simulation in the Trampedach grid is shown in Fig. 5. As can be seen from the figure, our new method appending $\langle 3D \rangle$ -envelopes on-the-fly reproduces the stratification of the 3D simulation reliably throughout the envelope, which agrees with the Stagger grid results in Paper I. It is clear that the Eddington grey atmosphere is very different from the 3D hydro-simulation. The *RT2014*-solar model using the 3D $T(\tau)$ relations and α_{MLT} mimics the correct structure above the photosphere, but deviates below – a similar results was found by Mosumgaard et al. (2018).

To assess the impact of using 3D information on the evolution, we continued the tracks from the solar calibrations up the

³ We have excluded one of these simulations where some quantities were apparently missing from the averaged data.

Table 1. Results from the different solar calibrations (here (3D)-envelope is based on the Trampedach grid; see text for further details). α_{MLT} denotes the mixing length, Y_1 is the initial helium mass fraction, Z_1 is the initial fraction of heavy elements, Y_s is the surface helium abundance, and $\frac{r_{\text{cz}}}{R_\odot}$ is the radius of the base of the convective envelope.

Model	α_{MLT}	Y_1	Z_1	Y_s	$\frac{r_{\text{cz}}}{R_\odot}$
Edd.	1.71	0.2680	0.0201	0.2388	0.7122
RT2014	1.82	0.2680	0.0201	0.2388	0.7122
(3D)-envelopes	5.36	0.2678	0.0200	0.2387	0.7122

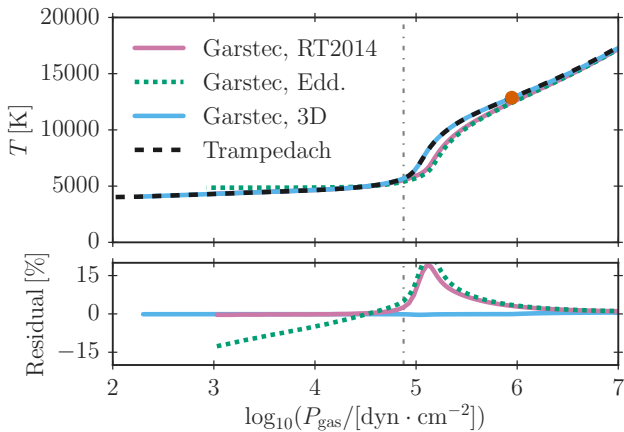


Figure 5. Comparison of the temperature as a function of gas pressure for the 3D solar simulation in the Trampedach grid (*Trampedach*) and the different solar calibrations from GARSTEC: *3D* is appending (3D)-envelopes from the Trampedach grid on-the-fly, *RT2014* is using a calibrated α_{MLT} and $T(\tau)$ relation from the same grid, and *Edd.* is performed with a standard grey Eddington boundary and constant α_{MLT} . The matching point of the (3D)-envelope-model is marked with a red dot. The residuals are with respect to the 3D solar simulation, in the sense *Trampedach* – *GARSTEC*. The dashed-dotted grey line indicates the position of the photosphere.

RGB. As shown by Mosumgaard et al. (2018), the use of the 3D calibrated $T(\tau)$ relation and α_{MLT} shifts the RGB towards higher effective temperatures compared to the regular Eddington case. As expected, we find the same qualitative trend for our implementation of (3D)-envelopes on-the-fly, as can be seen in Fig. 6, where the evolutionary tracks are shown alongside the 3D simulations from the Trampedach grid. In other words, models with a standard Eddington grey atmosphere have systematically lower T_{eff} on the RGB. The difference between the track appending (3D)-envelopes on-the-fly and the Eddington reference is around $\Delta T_{\text{eff}} \approx 55$ K at the RGB luminosity bump. This difference is somewhere between the RGB temperature offset at solar metallicity predicted by Tayar et al. (2017) and Salaris et al. (2018); it is also around the same magnitude as the shift found by the latter when changing between common $T(\tau)$ relation as boundary conditions for their models.

Moreover, Fig. 6 suggest that our new method leads to a kink at the base of the RGB – similar to what was seen in the previous section. We attribute this again to interpolation errors due to the even lower resolution of the Trampedach grid in this region. The morphology of the kink is somewhat different – more like a sharp break – which likely stems from the irregular sampling of the Trampedach grid (compared to the almost uniform Stagger grid).

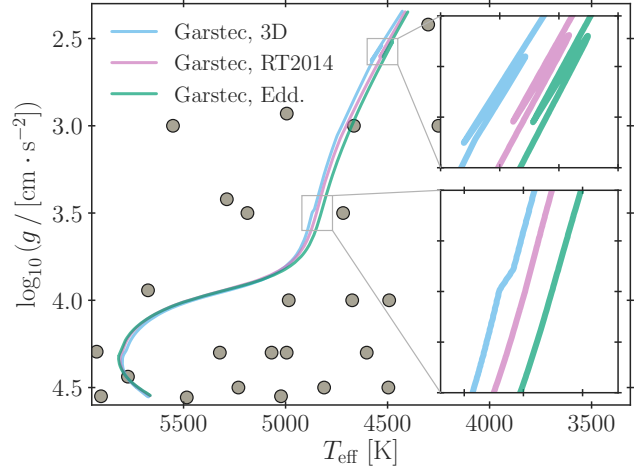


Figure 6. Evolutionary tracks for the solar models, with colors and labels corresponding to Fig. 5. The ticks on the zoomed insets correspond to 50 K and 0.05 dex, respectively. The grey dots show the location of a selection of the 3D simulations from the Trampedach grid.

As pointed out in Section 3.2, such kinks call for a refinement of the currently employed grids of 3D-envelopes – regardless of the specific grid. In the following section we will investigate the effects of the grid resolution in more detail.

As a final note, we repeated the full matching-depth analysis from Section 3.2 for the Trampedach grid. Bearing the slightly shallower Trampedach simulations in mind, we observe the same qualitative behaviour for this grid as we did for the Stagger grid (shown in Fig. 3). Specifically, α_{MLT} increases with increasing matching depth, reaching $\alpha_{\text{MLT}} = 17$ for a scaled pressure corresponding to a matching depth of $d_m = 0.95$ Mm for the present Sun. Regarding the frequencies as a function of matching depth, we observe the same trend as before: Below a certain depth – around $d_m = 0.5 - 0.6$ Mm which is similar to what was seen for the Stagger grid – the frequencies are virtually insensitive to the matching point. It should be noted that generally the agreement between the models frequencies and observations are worse in this case than for the Stagger grid, as a result of the different opacities and chemical mixture.

In the remainder of this paper, we will restrict ourselves to models that employ the Stagger grid rather than the Trampedach grid, when appending (3D)-envelopes on-the-fly.

4 STELLAR EVOLUTION

To analyse the applicability of our procedure, we have produced a grid of stellar models appending Stagger grid (3D)-envelopes on-the-fly along the entire evolution. The tracks are computed at solar metallicity with masses between $0.7 M_\odot$ and $1.3 M_\odot$. In the calculations, the matching point is fixed to a scaled pressure factor of $K_m = 1.20$, which is the same as in Section 3.1 and Paper I. The tracks use a fixed $\alpha_{\text{MLT}} = 3.86$ from the solar calibration with the corresponding depth from Section 3.2. A list of the input physics is provided in the final paragraph of Section 2.

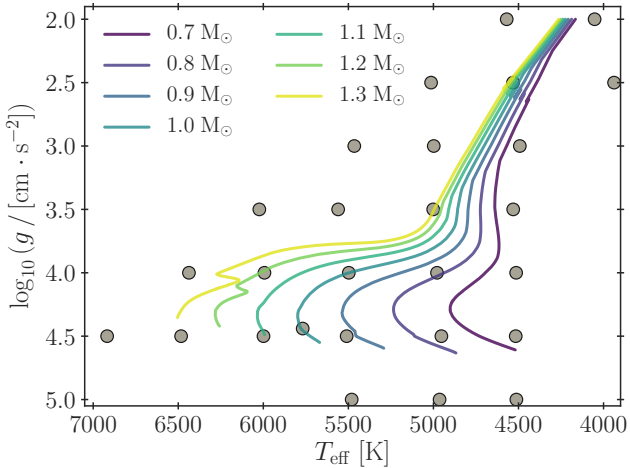


Figure 7. Evolutionary tracks for models with different stellar masses. The grey dots show the location of the Stagger grid models with solar metallicity.

4.1 Evolutionary tracks and grid resolution

A selected subset of the evolutionary tracks spanning the entire mass range of our grid is shown in Fig. 7 up to $\log g = 2.0$. As can be seen from the figure, the evolutionary sequences are generally well behaved, but show different kinks (or changes in slope) – especially visible on the RGB, but not at the same location for the different tracks.

The most prominent of these features are located between $\log g = 3.5$ and $\log g = 3.0$, which is in the same region of the Kiel diagram where difficulties emerged for the solar model tracks in Fig. 4. Similar kinks can be seen for the majority of the tracks between $\log g = 2.5$ and $\log g = 2.0$, and also in the main sequence for the $0.8 M_{\odot}$ and $0.9 M_{\odot}$ evolution. All of the cases are correlated with larger gaps in the Stagger grid – and also with movement of the simulation footpoints in the $(T_{\text{eff}}, \log g)$ -plane (see Appendix A). Thus, the bends generally occur on the virtual line between two of the simulations, i.e., when the tracks move to a different zone in the triangulation-based interpolation scheme (in either one of the two parameter spaces). Specifically, it seems to be a problem with the sampling of the underlying grid of 3D simulations.

To investigate the influence of the grid sampling, we performed numerous tests of the triangulation and interpolation. We modified the grid used by our routines in GARSTEC; specifically we tried degrading the grid by strategically removing some of the Stagger models. We also employed the code from J17 to compute new interpolated envelopes in the gaps (e.g. at $T_{\text{eff}} = 4775$, $\log g = 3.75$) to artificially refine the grid. All of the tests confirm the actual grid sampling to clearly affect the morphology of the RGB-kink: making the break smoother/sharper and more/less pronounced. The effect of the sampling in the different interpolation planes are discussed in Appendix A. To sum up, we need a denser grid of 3D hydro-simulations in order to produce smoother evolutionary sequences.

Fig. 7 illustrates the well-known effect that tracks are much closer to each other in temperature for the later evolutionary stages with lower surface gravities; at the zero-age main sequence (ZAMS) they span more than 2000 K, but this gets narrower moving up the RGB and the extent is less than 100 K at $\log g = 2.0$. In other words, during the main sequence the evolutionary tracks of different initial mass is spread across the entire grid, while the effective resolution

Table 2. Difference and relative deviation in T_{eff} at the photosphere and $\log g$ at the matching point, between the 1D stellar model and corresponding 3D simulation (in the sense 1D – 3D). The nomenclature specifies the surface parameters of the simulations: E.g. the model denoted $\tau 55g45$ has $T_{\text{eff}} = 5500$ K and $\log g = 4.5$.

Sim.	δT_{eff} [K]	$\delta T_{\text{eff}}/T_{\text{eff}}$	$\delta \log g$ [cgs]	$\delta \log g / \log g$
$\tau 45g25$	-0.535	-1.19×10^{-4}	-5.10×10^{-5}	-2.04×10^{-5}
$\tau 50g35$	-0.248	-4.96×10^{-5}	7.79×10^{-4}	2.23×10^{-4}
$\tau 55g40$	0.600	1.09×10^{-4}	7.83×10^{-4}	1.96×10^{-4}
$\tau 55g45$	0.810	1.47×10^{-4}	1.56×10^{-3}	3.47×10^{-4}
$\tau 60g40$	-0.360	-6.00×10^{-5}	-9.93×10^{-4}	-2.48×10^{-4}

is significantly reduced for red giants, with only a few simulations to cover the entire mass range. Another interesting observation is that the separation between the tracks decreases going up the RGB, whereas they are mostly parallel for standard evolution with an Eddington atmosphere. A potential future line of investigation would be to determine whether this is a true effect, or if it is due to a deficit in the low $\log g$ simulations, or a result of the RGB grid resolution.

Looking at the figure, a final important thing to keep in mind is that the applicability of our method is strongly determined by the parameter space covered by the 3D hydro-grid – both in terms of mass range and how far up the RGB the tracks can extend.

4.2 Structure at different evolutionary stages

Some of the evolutionary tracks contain models, where T_{eff} and $\log g$ correspond to one of the existing Stagger grid simulations – this is directly visible from Fig. 7, where some of the selected tracks pass through a dot. This facilitates an easy comparison between the obtained structure from the appended ⟨3D⟩-envelope in the stellar evolution model and the original 3D simulation. In other words, we want to verify that the direct output from our stellar structure model – including the quantities derived from the EOS – is consistent with the underlying full 3D simulations.

We have performed several of such comparisons, which are listed in Table 2 alongside the deviation in $\log g$ (at the matching point) and T_{eff} between the model and corresponding 3D simulation. The matching is within roughly 0.8 K and 10^{-3} dex, resulting in relative deviations at the 10^{-4} level or better. Especially the high precision in surface gravity at the matching point is important, as the interpolation is very sensitive to $\log g$. In the table, we have adopted the nomenclature from the Stagger grid to label the models: As an example, the model named $\tau 50g35$ has $T_{\text{eff}} = 5000$ K and $\log g = 3.5$.

The resulting residuals in temperature and density as a function of gas pressure for five cases are shown in Fig. 8 (using the same nomenclature), where the comparison of the Sun is added for reference. As can be seen from the top panel of the figure, our method reproduces the temperature stratification with high accuracy throughout the $(T_{\text{eff}}, \log g)$ -plane, with residuals below 0.2% above the matching point. The smallest residuals are seen for $\tau 45g25$, which has the best match to the simulation surface parameters. But generally we find no clear trends in the residuals with the deviation in matching parameters from Table 2.

Regarding the density – shown in the bottom panel of Fig. 8 – the procedure works particularly well for the main-sequence and subgiant stars in our sample, i.e., excluding the giant $\tau 45g25$ (discussed separately below). The residuals are within a few percent, which is very similar to the levels seen for the solar model in Paper

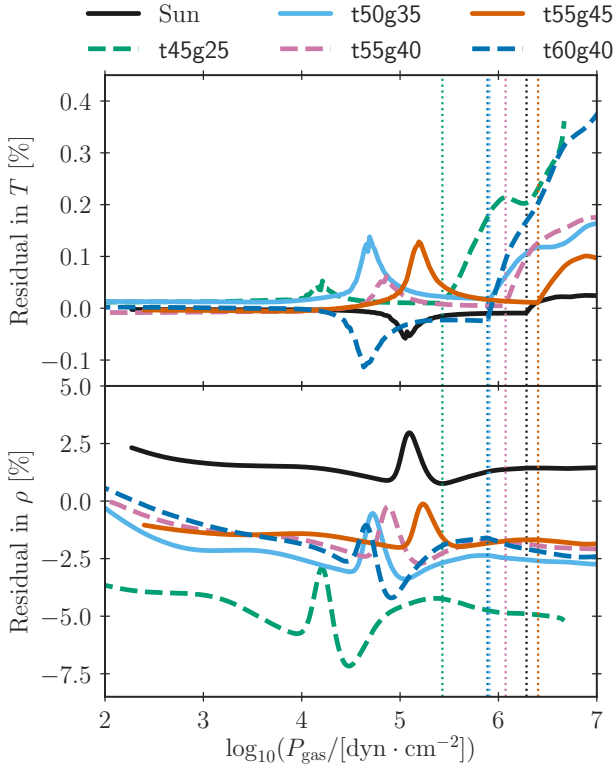


Figure 8. *Upper panel:* Comparison between the temperature stratification determined by GARSTEC and the corresponding Stagger grid simulation at solar metallicity for the selected cases of Table 2. The nomenclature is the same. The residuals are calculated as $3D\ simulation - GARSTEC$. For each set of surface parameters, a vertical dotted line with the corresponding color indicates the location of the matching point. *Lower panel:* As the upper panel but comparing the density stratification.

I. As for the temperature, we see no correlation of the residuals with how well the models match. Because the interpolation is entering only through the temperature stratification, the density residuals are not directly reflecting (additional) interpolation errors. As was also argued in Paper I, the discrepancies partly reflect the difference in EOS, but also the non-linearity of the thermodynamic quantities. Specifically, we derive the density from the mean of P_{gas} and T , i.e., $\rho(\langle P_{\text{gas}} \rangle, \langle T \rangle)$. Regardless of the EOS, this density is not expected to correspond exactly to the actual (geometrical) mean of the density, $\langle \rho(P_{\text{gas}}, T) \rangle$, in a 3D hydro-simulation, because the density is a non-linear function of pressure and temperature (Trampedach et al. 2014a).

For the more evolved giant shown (t45g25), the residuals in density between the Stagger grid simulation and outer parts of the stellar evolution model are somewhat larger – even though the level of the temperature residuals are not larger. The cause must be the above-mentioned difference in EOS and thermodynamic non-linearity, which clearly play a much larger role in the red-giant regime. Another possible contribution is a composition effect; however, this is unlikely to constitute the full part, because compared to the initial model in the sequence the difference is less than 0.01 in $[\text{Fe}/\text{H}]$ and around 0.02 in surface helium.

To sum up, the overall implementation is performing less well in the red-giant region of the parameter space. This is in line with the findings by J17, namely that the residuals in the patching grows

for the hottest and the most evolved stars. Thus, to fully utilize the potential of our method, more 3D simulations are required.

5 ASTEROSEISMIC APPLICATION

We want to investigate how our new procedure alters the results obtained from an asteroseismic analysis compared to a reference case. The selected stars must have an T_{eff} and $\log g$ inside the Stagger grid, and as we currently do not interpolate in metallicity, we are restricted to stars with a composition consistent with solar. Moreover, the method is expected to primarily perform well for cold main-sequence stars, as discussed above. Based on these restrictions, we have selected two stars from the *Kepler* asteroseismic LEGACY sample (Lund et al. 2017; Silva Aguirre et al. 2017) with large frequency separations around $\Delta\nu \sim 155 \mu\text{Hz}$: KIC 9955598 ($\Delta\nu = 153.3 \mu\text{Hz}$) and KIC 11772920 ($\Delta\nu = 157.7 \mu\text{Hz}$). The stellar parameters resulting from the fit (described in the next section) are listed in Table 3.

For the grid-based modelling analysis, two sets of stellar models have been computed: One appending $\langle 3D \rangle$ -envelopes from the Stagger grid on-the-fly and a reference grid with an Eddington grey atmosphere. The model grids contain the same microphysics as listed in Section 2, but do not include microscopic diffusion. The grid appending $\langle 3D \rangle$ -envelope on-the-fly uses $\alpha_{\text{MLT}} = 3.86$ (the $K_{\text{m}} = 1.20$ solar calibration from Section 3.2), while the Eddington solar calibration yields $\alpha_{\text{MLT}} = 1.80$.

The grids have been calculated with GARSTEC and span the mass range $M = 0.8 - 0.95 M_{\odot}$ in steps of $0.001 M_{\odot}$. For all models in the grids, ADIPLS (Christensen-Dalsgaard 2008) has been utilised to calculate individual oscillation frequencies.

5.1 Determined stellar parameters

To compare the observations to the calculated stellar models we have used BASTA (BAyesian STellar Algorithm, Silva Aguirre et al. 2015, 2017), which utilises both classical observables and asteroseismic data. Based on the observed quantities, the likelihood of all models in the grid is determined, and probability distributions and correlations constructed for the desired parameters. The reported values are the medians from these distributions with the 68.3 percentiles as corresponding uncertainties.

One way of using the asteroseismic data is to compare the observed individual oscillation frequencies $\nu_{n,l}$ to those computed from the models. Usually this approach requires an analytical prescription to correct for the surface effect (e.g., Kjeldsen et al. 2008; Ball & Gizon 2014). It should be noted that the exact shape of this correction is not known for our new stellar models appending $\langle 3D \rangle$ -envelopes on-the-fly, where the surface effect has been partly eliminated.

Another option is to use combinations of frequencies instead of the individual frequencies; specifically the frequency separation ratios defined as (Roxburgh & Vorontsov 2003):

$$r_{01}(n) = \frac{\nu_{n-1,0} - 4\nu_{n-1,1} + 6\nu_{n,0} - 4\nu_{n,1} + \nu_{n+1,0}}{8(\nu_{n,1} - \nu_{n-1,1})},$$

$$r_{10}(n) = \frac{-\nu_{n-1,1} + 4\nu_{n,0} - 6\nu_{n,1} + 4\nu_{n+1,0} - \nu_{n+1,1}}{8(\nu_{n+1,0} - \nu_{n,0})},$$

$$r_{02}(n) = \frac{\nu_{n,0} - \nu_{n-1,2}}{\nu_{n,1} - \nu_{n-1,1}}.$$

These frequency separation ratios have been shown to be less sensitive to the outer layers and primarily probe the interior of the star

(see, e.g., Oti Floranes et al. 2005; Roxburgh 2005), and thus eliminate the need for a correction of the surface term. Typically the ratios are combined into a set of observables, e.g.:

$$r_{010} = \{r_{01}(n), r_{10}(n), r_{01}(n+1), r_{10}(n+1), \dots\}.$$

To test the consistency of our new models, we used BASTA to estimate the stellar properties based on a fit to the spectroscopic temperature and the frequency ratios r_{010} and r_{02} .⁴ In the current context, the agreement between the two fits and not the actual parameter values is our primary concern. However, to guide the discussion the inferred stellar parameters from both sets of models are listed in Table 3.

In general, the resulting parameters from the grid of ⟨3D⟩-envelope models and the grid of Eddington models show good agreement. The effective temperature is particularly interesting, as we know from an earlier section that the T_{eff} evolution can be different between the two sets of models. However, not much is predicted to change on main sequence; as expected, for KIC 9955598 the two values are within the uncertainties of each other, while for KIC 11772920 the quoted uncertainty bands in T_{eff} overlap. For both stars, for all of the remaining parameters – mass, radius and age – the agreement between the two grids is even better, and within half a standard deviation of each other.

After verifying the consistency with the non-surface dependent separation ratios, we repeated the procedure using instead the individual oscillation frequencies. We assume the two-term surface correction from Ball & Gizon (2014) and fit the stars using the same two sets of models. The inferred parameters from this analysis are not shown; however they are similar to the presented results from the fit to the r_{010} and r_{02} ratios. The determined parameters from the Eddington and the ⟨3D⟩-envelope grid show the same level of agreement as above, i.e., less than half a standard deviation for all of the parameters except T_{eff} . Moreover, all of the fits to the same star using the different sets of asteroseismic observables are internally consistent, too.

5.2 The surface effect

Besides estimating the stellar parameters, we want to investigate the impact on the important asteroseismic surface effect. In order to isolate the surface term, we add an additional assumption to our fitting: The model must match the observed lowest order $\ell = 0$ mode within 3σ . From BASTA we can get the full stellar model corresponding to the point with the highest assigned likelihood – given our extra assumption – also known as the best-fitting model (BFM). By comparing the BFM from each grid, we can investigate if our new models alters the individual oscillation frequencies.

In Fig. 9, the BFM-comparison for KIC 11772920 is shown in the form of frequency difference with respect to the observations. Looking at the figure, it is clear that the frequencies of our new model appending ⟨3D⟩-envelopes on-the-fly deviates less from the observations, without the need of a surface correction.

The figure likewise contains two patched models (PM) constructed following the procedure described by Paper I and J17. The base model for the present patching exercise is the GARSTEC model

⁴ The use of the r_{010} in combination with r_{02} was disputed by Roxburgh (2018), due to the risk of overfitting the data, and instead suggested using the single series r_{102} (or r_{012}). Using the r_{012} in BASTA, we obtain parameters fully consistent with the ‘standard’ ratios fit.

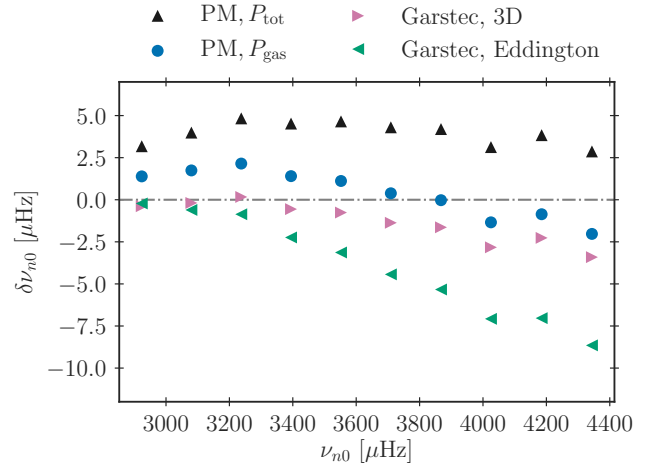


Figure 9. Frequency differences between predicted $\ell = 0$ model frequencies and observations for KIC 11772920. The plot includes the best-fitting model with an Eddington grey atmosphere and with Stagger grid ⟨3D⟩-envelopes on-the-fly. Based on the latter, we have furthermore constructed two patched models (PM): one, for which the total pressure (P_{tot}) enters the computation of the depth scale, using hydrostatic equilibrium, and one, for which only the gas pressure P_{gas} is used to compute r .

employing our new implementation. In each case we have substituted the outer layers of this model with the full ⟨3D⟩-structure of an interpolated Stagger grid envelope with the same T_{eff} and $\log g$. The first case – denoted as “PM, P_{tot} ” in the figure – is taken as it is, i.e., it includes turbulent pressure in the patched layers. In the second case, which is dubbed “PM, P_{gas} ”, the depth scale of the patched ⟨3D⟩-envelope is recalculated solely based on the gas pressure.

Since our GARSTEC implementation neglects turbulent pressure and infers ρ and Γ_1 from the EOS, especially the first case substitution is expected to alter the structure and affect the model frequencies (cf. e.g. Paper I and Jørgensen & Weiss 2019). To facilitate a meaningful comparison with the frequencies from stellar evolution models, we do not include the contribution from turbulent pressure in the oscillation equations for this PM, i.e., we assume “gas Γ_1 approximation” in the nomenclature of Rosenthal et al. (1999). For an elaboration of this see Paper I (Sec. 3.2) and Houdek et al. 2017.

From Fig. 9 we see that including the turbulent pressure in the patched exterior give rise to model frequencies which are 4 – 7 μHz lower than the frequencies of the underlying GARSTEC model. Note that the so-called *modal effects* – including non-adiabatic contributions in the computation of the mode frequencies in the separate pulsation code (ADIPLS) – are not included in the current treatment, but would still play a significant role for the remaining discrepancy (Houdek et al. 2017).

When recomputing the depth scale of the patched ⟨3D⟩-envelope purely based on the gas pressure, this mismatch in the oscillations is reduced to $\lesssim 2 \mu\text{Hz}$. This illustrates the importance of taking turbulent pressure properly into account. The remaining discrepancy between the PM and the model that has been obtained, using our new implementation, may partly be attributed to a mismatch in the stratification of ρ or Γ_1 – that is, frequency differences may be attributed to the EOS or assumptions made by the EOS. Furthermore, this discrepancy may partly reflect interpolation errors.

Moving on to the other case, KIC 9955598, we return to the surface effect and the stellar evolution models. The frequencies of

Table 3. Parameters of the modelled *Kepler* stars, appending ⟨3D⟩-envelope on-the-fly (*Stag.*), or using Eddington grey atmospheres (*Edd.*) as boundary conditions. Inferred using BASTA (details in the text). The listed values correspond to the median of the obtained probability distributions from BASTA and the uncertainties denote 68.3% Bayesian credibility intervals.

KIC	Model	T_{eff} [K]	$\log g$ [cgs]	Mass [M_{\odot}]	R_{phot} [R_{\odot}]	Age [Myr]
9955598	<i>Edd.</i>	5572^{+13}_{-13}	$4.4983^{+0.0011}_{-0.0012}$	$0.897^{+0.005}_{-0.005}$	$0.8839^{+0.0021}_{-0.0019}$	6997^{+360}_{-349}
9955598	<i>Stag.</i>	5584^{+10}_{-10}	$4.4989^{+0.0011}_{-0.0012}$	$0.899^{+0.004}_{-0.005}$	$0.8840^{+0.0019}_{-0.0019}$	6944^{+352}_{-322}
11772920	<i>Edd.</i>	5423^{+15}_{-15}	$4.5061^{+0.0013}_{-0.0013}$	$0.849^{+0.005}_{-0.006}$	$0.8520^{+0.0023}_{-0.0023}$	9874^{+528}_{-499}
11772920	<i>Stag.</i>	5449^{+16}_{-16}	$4.5069^{+0.0013}_{-0.0013}$	$0.852^{+0.006}_{-0.006}$	$0.8529^{+0.0023}_{-0.0022}$	9752^{+510}_{-506}

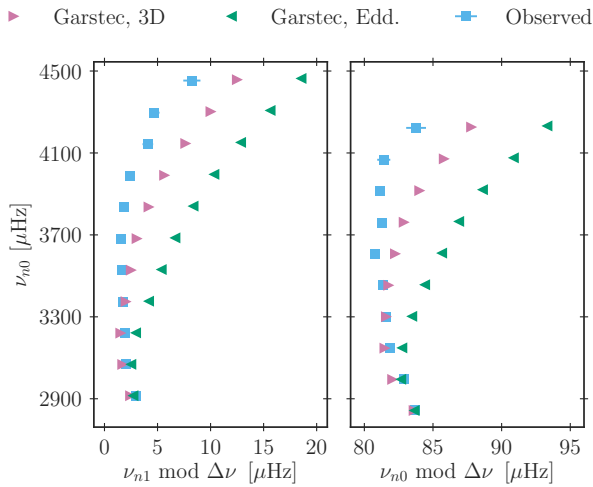


Figure 10. Échelle diagrams of KIC 9955598 for $\ell = 0$ (right) and $\ell = 1$ (left). Model frequencies are from the best-fitting model obtained with BASTA, using the two different grids of stellar models with Eddington atmospheres and ⟨3D⟩-envelopes on-the-fly, respectively (details in the text)

the two BFM’s – obtained from the grid-based fit with an additional constraint on the lowest $\ell = 0$ mode – and the observations of KIC 9955598 can be seen in Fig. 10. The comparison is shown in the form of échelle diagrams for two different radial orders. From the figure it is very clear that the model appending ⟨3D⟩-envelopes on-the-fly has frequencies deviating significantly less from the observed values for both orders. All in all, compared to canonical stellar evolution models, the oscillation frequencies from our new models are much closer to the observations, without the use of any sort of correction for the surface term.

6 RED-GIANT BRANCH MODELS

In line with the previous section, we investigate further the asteroseismic implications of our new method, focusing here on the solar-like acoustic oscillations in red-giant stars and how the surface effect changes. Red giants are very important for many astrophysical fields, e.g. for probing distant regions in the Galaxy or studying star clusters. The analysis of such stars has matured rapidly in the era of space-based photometry and asteroseismology with *CoRoT* (Baglin et al. 2009) and *Kepler* (Borucki et al. 2010; Gilliland et al. 2010), but the modelling deficiencies in the near surface layers are still not well understood.

In order to perform a detailed differential frequency analysis of two stellar models, the two must be very similar seismically. It is natural to compare models of identical mean density, which is correlated with the asteroseismic large frequency separation $\Delta\nu$ (Ulrich 1986). To ensure this, we adopted the convergence criterion devised for the *Aarhus Red Giants Challenge*⁵ (Silva Aguirre et al., submitted; Christensen-Dalsgaard et al., submitted). For a given model (*mod*) the minimum acceptable convergence at *a* solar masses and *b* solar radii is defined as

$$\Delta_{\text{convergence}} = \left| 1 - \frac{G_{\text{mod}} M_{\text{mod}} / R_{\text{mod}}^3}{G(a \times M_{\odot}) / (b \times R_{\odot})^3} \right| \leq 2 \times 10^{-4}, \quad (2)$$

where *G* is the gravitational constant. The choice of 2×10^{-4} is a compromise between the uncertainties in the asteroseismic frequencies and the ease of finding the required model, as discussed by Silva Aguirre et al. (submitted).

For models calculated with the same stellar evolution code, *G* is of course invariant and the convergence is solely determined by the mass and radius. For the model to match a reference model with the desired radius R_{ref} , the criterion can be rewritten and reduced to

$$\Delta_{\text{convergence}} = \left| 1 - \frac{M_{\text{mod}} R_{\text{ref}}^3}{M_{\text{ref}} R_{\text{mod}}^3} \right| \leq 2 \times 10^{-4}, \quad (3)$$

where M_{ref} is the mass of the reference model at radius R_{ref} .

For this analysis we use the same settings in the computations as in Section 4 and 5 – i.e. like those listed in Section 2, but without microscopic diffusion – and two initial masses: 1.00 and 1.30 M_{\odot} . Like in the previous section, two different sets of models were calculated: One appending Stagger ⟨3D⟩-envelopes on-the-fly and another using a standard Eddington $T(\tau)$ relation. The models with Stagger ⟨3D⟩-envelopes are taken as the reference model in eq. (3) and the Eddington model is carefully calculated to match within the convergence limit. For the comparison we selected RGB models at different surface gravity positions – $\log g = 3.0$, $\log g = 2.5$, and $\log g = 2.0$ – and an overview can be seen in Table 4 (alongside the results described below).

For a set of matching models, the oscillation frequencies are computed with ADIPLS and compared. An example of the frequency difference comparison for models with $M = 1.00 M_{\odot}$ at $R = 9.32 R_{\odot}$ is shown in Fig. 11. For the other comparison points, the shape of the differences looks almost identical, albeit with lower frequencies and fewer modes the lower $\log g$ gets.

⁵ A series of workshops dedicated to modelling of red-giant stars and especially to detailed comparisons of many different stellar evolution codes.

Table 4. Comparison points for RGB models. The convergence in radius is according to eq. (3) with Stagger (3D)-envelopes on-the-fly as the reference, and Eddington computed to match. The frequency of maximum oscillation power, ν_{\max} , is determined from the Stagger models using eq. (4). The frequency difference is “3D – Eddington” and determined as a 3-point average around ν_{\max} (see the text for details).

M [M_{\odot}]	$\log g$	R [R_{\odot}]	ν_{\max} μHz	$\delta\nu_{\nu_{\max}}$ μHz	$\delta\nu_{\nu_{\max}}/\nu_{\max}$
1.00	3.0	5.24	124.49	-0.510	-4.10×10^{-3}
1.00	2.5	9.32	40.34	-0.309	-7.67×10^{-3}
1.00	2.0	16.47	13.31	-0.097	-7.31×10^{-3}
1.30	3.0	5.97	123.75	-0.564	-4.56×10^{-3}
1.30	2.5	10.63	40.10	-0.228	-5.70×10^{-3}
1.30	2.0	18.89	13.11	-0.104	-7.95×10^{-3}

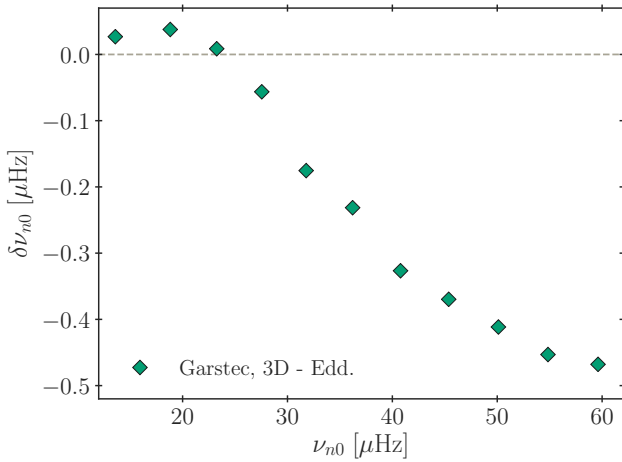


Figure 11. Frequency difference between calculated $\ell = 0$ frequencies for the model with (3D)-envelopes appended on-the-fly and standard Eddington model with initial masses of $1.00 M_{\odot}$, as a function of (3D)-envelope frequencies. The comparison point is chosen near $\log g = 2.5$ at $R = 9.32 R_{\odot}$.

To quantify this, and to compare the actual shape of the deviation between the different comparison points, we need to scale the quantities. Thus, we calculate the frequency of maximum oscillation power, ν_{\max} , using the scaling relation from [Kjeldsen & Bedding \(1995\)](#),

$$\frac{\nu_{\max}}{\nu_{\max,\odot}} \simeq \left(\frac{M}{M_{\odot}}\right) \left(\frac{R}{R_{\odot}}\right)^2 \left(\frac{T_{\text{eff}}}{T_{\text{eff},\odot}}\right)^{-1/2}, \quad (4)$$

where \odot denotes the solar values, and specifically $\nu_{\max,\odot} = 3090 \mu\text{Hz}$. For a given set of converged models, ν_{\max} is calculated using the quantities of the (3D)-envelope model – due to the convergence defined by eq. (3), ν_{\max} of the two models in a pair are almost identical, with the variation caused by the differences in T_{eff} (on the order of 40 K). Then we select the oscillation mode closest to ν_{\max} and the two adjacent modes – one on either side – and calculate the average frequency deviation of these three modes, which we denote $\delta\nu_{\nu_{\max}}$. Now, the frequencies are scaled by ν_{\max} and the frequency differences by $\delta\nu_{\nu_{\max}}$.

All of the quantities are listed in Table 4, and in all cases the relative difference at the frequency of maximum power is below 1%. Additionally, four of the resulting curves – which turns out to be remarkably similar – are shown in Fig. 12. From this figure, it is clear that the shape of the deviation is independent of position on the RGB, and equally important independent of mass as well.

As also mentioned in the introduction, the application of atmo-

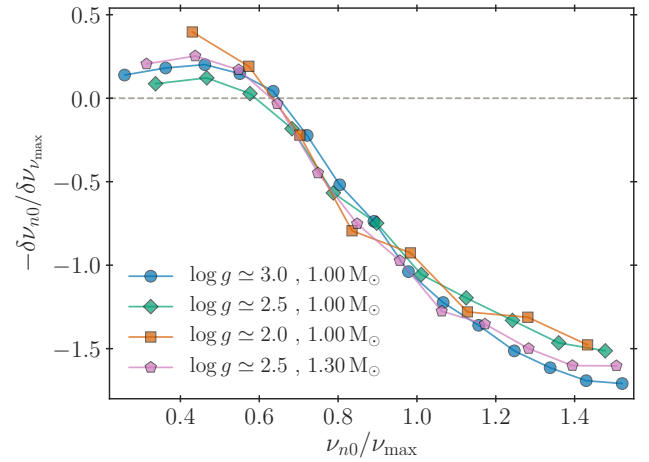


Figure 12. Scaled frequency differences (“3D – Eddington”) for several RGB models. For a given comparison, the model frequencies and frequency differences are scaled by respectively the frequency of maximum oscillation power, ν_{\max} , and the difference at this point, $\delta\nu_{\nu_{\max}}$ (details in the text) The green diamonds are identical to those in Fig. 11, except for the applied scaling. All quantities and comparison points are listed in Table 4

spheric 3D hydro-simulations to study the surface effect of solar-like oscillators has been the focus of different studies in the recent years. Several groups have utilized the patched model technique to perform investigations across the HR (or Kiel) diagram. One to highlight in the current context is the work by [Sonoji et al. \(2015\)](#), because two of their comparison points are denoted as red giants: Their model I ($T_{\text{eff}} = 5885 \text{ K}$, $\log g = 3.5$) and model J ($T_{\text{eff}} = 4969 \text{ K}$, $\log g = 2.5$). Even though it is somewhat hotter, the latter is especially interesting for our comparison being furthest up the RGB. Note, however, that the performed patch for J is using a $M = 3.76 M_{\odot}$ model, which is very different from our cases.) They derive corrections both in the form of the classical [Kjeldsen et al. \(2008\)](#) power law and their own “modified Lorentzian formulation”, where one of the quantities in both fits can be directly translated to $\delta\nu/\nu_{\max}$ at $\nu = \nu_{\max}$ (denoted $\delta\nu_{\nu_{\max}}/\nu_{\max}$ above). We predict the same sign of the deviation and, taking the quite different approaches into account, our results are roughly of the same magnitude. Furthermore, their equation 10 provides the fitting factors as a function of $\log g$ and T_{eff} ; we do not see a clear surface gravity trend as they predict, but the magnitude of the estimates from this is also in line with our findings.

However, as very recently shown by [Jørgensen et al. \(2019\)](#) based on an analysis of 315 patched models, the coefficients in the

Lorentzian formulation by [Sonoii et al. \(2015\)](#) strongly depend on the underlying sample. Consequently, there exists no set of coefficient values that is universally applicable throughout the parameter space. The authors note that the formulation derived by [Sonoii et al. \(2015\)](#) suffers from a selection bias, as it is predominantly based on models, for which $T_{\text{eff}} > 6000$ K and $\log g \geq 4.0$. It follows that their fit cannot be directly applied to stars on the RGB. Our current results are in line with this conclusion.

Finally, we note that neither the Lorentzian formulation by [Sonoii et al. \(2015\)](#) nor the frequency difference we present in Fig. 12 can be directly translated into a surface correction relation, since modal effects and turbulent pressure have been neglected.

7 CONCLUSIONS

We have presented an extensive analysis of stellar models that append $\langle 3D \rangle$ -envelopes on-the-fly from the Stagger grid ([Magic et al. 2013](#)) at each time step, following the procedure introduced by Paper I. These models provide a more physically accurate description of the outermost layers in low-mass stars.

When calculating the appended $\langle 3D \rangle$ -envelopes, we use the equation of state from the stellar evolution code. In Paper I, we verified that the density and temperature obtained from the equation of state showed good agreement with the 3D solar simulation. Here we verified that the resulting first adiabatic index Γ_1 does not significantly shift the obtained oscillation frequencies compared to using Γ_1 directly from the 3D simulation.

By performing different solar calibrations, we investigated the effect of the so-called matching point, i.e., the depth above which the $\langle 3D \rangle$ -envelopes are appended to the stellar model. We find the mixing length to increase monotonically with increasing matching depth, which is in qualitative agreement with [Schlattel et al. \(1997\)](#). This being said, the evolutionary tracks are relatively insensitive to the matching point, provided that it is placed sufficiently deep within the superadiabatic outer layers. Moreover, we find that the oscillation frequencies are equally independent of the matching depth for sufficiently high values.

We have performed a solar model analysis using the grid of 3D simulations computed by [Trampedach et al. \(2013\)](#), and find consistency with the Stagger grid results (shown in Paper I). Moreover, the computed evolutionary tracks are shifted towards higher effective temperatures on the red-giant branch (RGB) compared to reference Eddington-grey models. The same qualitative effect was found by [Mosumgaard et al. \(2018\)](#) utilising parametrised information from the same 3D grid extracted by [Trampedach et al. \(2014a,b\)](#).

Moving on from the Sun, we have computed evolutionary tracks for stars of different mass to further test our procedure for including $\langle 3D \rangle$ -envelope on-the-fly. The tracks show prominent kinks at the boundaries of the grid of 3D simulations, as well as in regions where the sampling is sparse – especially problematic on the RGB and in the PMS. This calls for a refinement of the 3D grids to make the interpolation more reliable (see also J17). Furthermore, more simulations at higher temperatures will extend the usefulness of our method by widening the allowed mass range.

Moreover, we took advantage of the different models across the $(T_{\text{eff}}, \log g)$ -plane to further investigate the applicability of our method and specifically the equation of state. By comparing to full 3D simulation, we can conclude that the density is reproduced accurately for main sequence stars and subgiants; however the residuals are slightly larger for more evolved giants. This is partially a reso-

lution effect, due to the very few simulations along the RGB, where the tracks are close to each other.

For the first time, an asteroseismic analysis using stellar models including $\langle 3D \rangle$ -envelope on-the-fly is presented. Using a grid-based approach and the Bayesian inference code *BASTA* ([Silva Aguirre et al. 2015](#)), we determined the stellar parameters of two stars from the *Kepler* LEGACY sample ([Lund et al. 2017](#); [Silva Aguirre et al. 2017](#)). We find that the obtained parameters are consistent – in the sense that they agree within the uncertainties – between the grid with our new method and the reference Eddington case. This consistency also holds between fits to individual frequencies and frequency separation ratios. Furthermore, comparing the best-fitting models from both grids to the observations, we see that the asteroseismic surface effect is strongly reduced by using $\langle 3D \rangle$ -envelopes on-the-fly. In other words, our new models are able to predict frequencies much closer to observations without using any additional corrections – and are able to do so consistently across stellar parameters.

Finally, we extended the asteroseismic investigation to red giants. We carefully matched standard Eddington models with $\langle 3D \rangle$ -envelopes appended on-the-fly to look at the detailed differences in their oscillation frequencies. We see a relative difference below 1% at the frequency of maximum power, and no trend in shape or relative deviation with either mass or surface gravity.

Although the differences between the new models and the patched ones – and even the Eddington-grey ones (besides the surface term) – are rather minor, we have demonstrated the robustness of the method with regard to details of the application of the $\langle 3D \rangle$ -envelopes, both for main-sequence and red-giant stars. We expect larger effects for lower metallicity red giants, which we treat in a future work. As a last remark, we want to once again stress the need for a denser grid of 3D atmospheres/envelopes, and the requirement to compute new hydrodynamical simulations to achieve this. This will enable the use of $\langle 3D \rangle$ -envelopes on-the-fly for stellar evolution – to obtain more realistic models – to reach its full potential.

ACKNOWLEDGEMENTS

We thank the anonymous referee for the thorough review and useful suggestions, which have improved the presentation of the paper. We give our thanks to R. Trampedach for many insightful discussions, his opinion on technical matters and for providing us with his grid of simulations. We also record our gratitude to R. Collet, Z. Magic and H. Schlattel for a fruitful collaboration. We acknowledge the funding we received from the Max-Planck Society, which is much appreciated. Funding for the Stellar Astrophysics Centre is provided by the Danish National Research Foundation (grant DNR106). ACSJ acknowledges the IMPRS on Astrophysics at the Ludwig-Maximilians University. VSA acknowledges support from VILLUM FONDEN (research grant 10118) and the Independent Research Fund Denmark (Research grant 7027-00096B). This research was partially conducted during the Exostar19 program at the Kavli Institute for Theoretical Physics at UC Santa Barbara, which was supported in part by the National Science Foundation under Grant No. NSF PHY-1748958

REFERENCES

- Asplund M., Grevesse N., Sauval A. J., Scott P., 2009, *Annual Review of Astronomy and Astrophysics*, 47, 481
 Badnell N. R., Bautista M. A., Butler K., Delahaye F., Mendoza C., Palmeri

- P., Zeppen C. J., Seaton M. J., 2005, *Monthly Notices of the Royal Astronomical Society*, 360, 458
- Baglin A., Auvergne M., Barge P., Deleuil M., Michel E., CoRoT Exoplanet Science Team 2009, *Proceedings of the International Astronomical Union*, 253, 71
- Ball W. H., Gizon L., 2014, *Astronomy & Astrophysics*, 568, A123
- Ball W. H., Beeck B., Cameron R. H., Gizon L., 2016, *Astronomy & Astrophysics*, 592, A159
- Basu S., Antia H. M., 1997, *Monthly Notices of the Royal Astronomical Society*, 287, 189
- Basu S., Antia H. M., 2004, *The Astrophysical Journal*, 606, L85
- Biermann L., 1932, *Z. Astrophys.*, 5, 117
- Böhm-Vitense E., 1958, *Zeitschrift für Astrophysik*, 46, 108
- Borucki W. J., et al., 2010, *Science*, 327, 977
- Broomhall A.-M., Chaplin W. J., Davies G. R., Elsworth Y., Fletcher S. T., Hale S. J., Miller B., New R., 2009, *Monthly Notices of the Royal Astronomical Society: Letters*, 396, L100
- Brown T. M., 1984, *Science*, 226, 687
- Cassisi S., Salaris M., Irwin A. W., 2003, *The Astrophysical Journal*, 588, 862
- Christensen-Dalsgaard J., 2002, *Reviews of Modern Physics*, 74, 1073
- Christensen-Dalsgaard J., 2008, *Astrophysics and Space Science*, 316, 113
- Christensen-Dalsgaard J., Gough D., 1984, in Ulrich R. K., Harvey J., Rhodes E. J. J., Toomre J., eds, *Solar Seismology from Space*. pp 199–204
- Christensen-Dalsgaard J., Däppen W., Lebreton Y., 1988, *Nature*, 336, 634
- Cox J. P., Giuli R. T., 1968, *Principles of stellar structure*. New York: Gordon and Breach
- Davies G. R., Broomhall A.-M., Chaplin W. J., Elsworth Y., Hale S. J., 2014, *Monthly Notices of the Royal Astronomical Society*, 439, 2025
- Ferguson J. W., Alexander D. R., Allard F., Barman T., Bodnarik J. G., Hauschildt P. H., Heffner-Wong A., Tamanai A., 2005, *The Astrophysical Journal*, 623, 585
- Gilliland R. L., et al., 2010, *PASP*, 122, 131
- Gough D. O., Weiss N. O., 1976, *MNRAS*, 176, 589
- Houdek G., Trampedach R., Aarslev M. J., Christensen-Dalsgaard J., 2017, *Monthly Notices of the Royal Astronomical Society: Letters*, 464, L124
- Iglesias C. A., Rogers F. J., 1996, *The Astrophysical Journal*, 464, 943
- Jørgensen A. C. S., Weiss A., 2019, *Monthly Notices of the Royal Astronomical Society*, 488, 3463
- Jørgensen A. C. S., Weiss A., Mosumgaard J. R., Silva Aguirre V., Sahlholdt C. L., 2017, *Monthly Notices of the Royal Astronomical Society*, 472, 3264
- Jørgensen A. C. S., Mosumgaard J. R., Weiss A., Silva Aguirre V., Christensen-Dalsgaard J., 2018, *MNRAS*, 481, L35
- Jørgensen A. C. S., Weiss A., Angelou G., Silva Aguirre V., 2019, *MNRAS*, 484, 5551
- Kippenhahn R., Weigert A., Weiss A., 2012, *Stellar Structure and Evolution*, 2 edn. Springer-Verlag Berlin Heidelberg
- Kjeldsen H., Bedding T. R., 1995, *A&A*, 293, 87
- Kjeldsen H., Bedding T. R., Christensen-Dalsgaard J., 2008, *The Astrophysical Journal*, 683, L175
- Lund M. N., et al., 2017, *The Astrophysical Journal*, 835, 172
- Magic Z., Weiss A., 2016, *Astronomy & Astrophysics*, 592, A24
- Magic Z., Collet R., Asplund M., Trampedach R., Hayek W., Chiavassa A., Stein R. F., Nordlund Å., 2013, *Astronomy & Astrophysics*, 557, A26
- Mosumgaard J. R., Silva Aguirre V., Weiss A., Christensen-Dalsgaard J., Trampedach R., 2017, in Monteiro M., Cunha M., Ferreira J., eds, *EPJ Web of Conferences* Vol. 160, *Seismology of the Sun and the Distant Stars II*. p. 03009, doi:10.1051/epjconf/201716003009
- Mosumgaard J. R., Ball W. H., Silva Aguirre V., Weiss A., Christensen-Dalsgaard J., 2018, *Monthly Notices of the Royal Astronomical Society*, 478, 5650
- Nordlund Å., Stein R. F., Asplund M., 2009, *Living Reviews in Solar Physics*, 6, 2
- Otí Floranes H., Christensen-Dalsgaard J., Thompson M. J., 2005, *Monthly Notices of the Royal Astronomical Society*, 356, 671
- Pedersen B. B., Vandenberg D. A., Irwin A. W., 1990, *The Astrophysical Journal*, 352, 279
- Piau L., Collet R., Stein R. F., Trampedach R., Morel P., Turck-Chièze S., 2014, *Monthly Notices of the Royal Astronomical Society*, 437, 164
- Rosenthal C. S., Christensen-Dalsgaard J., Nordlund Å., Stein R. F., Trampedach R., 1999, *Astronomy and Astrophysics*, 351, 689
- Roxburgh I. W., 2005, *Astronomy & Astrophysics*, 434, 665
- Roxburgh I. W., 2018, arXiv e-prints, p. arXiv:1808.07556
- Roxburgh I. W., Vorontsov S. V., 2003, *a&a*, 411, 215
- Salaris M., Cassisi S., 2008, *Astronomy & Astrophysics*, 487, 1075
- Salaris M., Cassisi S., 2015, *Astronomy & Astrophysics*, 577, A60
- Salaris M., Cassisi S., Schiavon R. P., Pietrinferni A., 2018, *Astronomy & Astrophysics*, 612, A68
- Schlattl H., Weiss A., Ludwig H.-G., 1997, *Astronomy and Astrophysics*, 322, 646
- Silva Aguirre V., et al., 2015, *Monthly Notices of the Royal Astronomical Society*, 452, 2127
- Silva Aguirre V., et al., 2017, *The Astrophysical Journal*, 835, 173
- Sonoi T., Samadi R., Belkacem K., Ludwig H.-G., Caffau E., Mosser B., 2015, *Astronomy & Astrophysics*, 583, A112
- Stein R. F., Nordlund Å., 1989, *The Astrophysical Journal*, 342, L95
- Stein R. F., Nordlund Å., 1998, *The Astrophysical Journal*, 499, 914
- Tayar J., et al., 2017, *The Astrophysical Journal*, 840, 17
- Trampedach R., 2010, *Ap&SS*, 328, 213
- Trampedach R., Asplund M., Collet R., Nordlund Å., Stein R. F., 2013, *The Astrophysical Journal*, 769, 18
- Trampedach R., Stein R. F., Christensen-Dalsgaard J., Nordlund Å., Asplund M., 2014a, *Monthly Notices of the Royal Astronomical Society*, 442, 805
- Trampedach R., Stein R. F., Christensen-Dalsgaard J., Nordlund Å., Asplund M., 2014b, *Monthly Notices of the Royal Astronomical Society*, 445, 4366
- Trampedach R., Aarslev M. J., Houdek G., Collet R., Christensen-Dalsgaard J., Stein R. F., Asplund M., 2017, *Monthly Notices of the Royal Astronomical Society*, 466, L43
- Ulrich R. K., 1986, *ApJ*, 306, L37
- Vitense E., 1953, *Zeitschrift für Astrophysik*, 32, 135
- Weiss A., Schlattl H., 2008, *Astrophysics and Space Science*, 316, 99

APPENDIX A: GRID MORPHOLOGY

The Stagger grid is designed with spectroscopy in mind and is therefore regular in the Kiel diagram, i.e., in the $(T_{\text{eff}}, \log g)$ -plane. However, as described in the paper, we also need to set up a triangulation in the $(T_m, \log g)$ -space, where T_m is the temperature at the matching point given the choice of K_m . This is required by our implementation in order to infer T_{eff} by interpolation.

In Section 3.2 and Section 4.1, it was discussed that the effective resolution of Stagger grid in the $(T_m, \log g)$ -plane is different from the almost-regular $(T_{\text{eff}}, \log g)$ -space. This is an effect of the given simulation points moving as a function of K_m .

In the top panel of Fig. A1, the Stagger grid at solar metallicity is shown in the traditional Kiel diagram. To ease the discussion, the individual simulation is annotated with a number – 1 for the lowest T_{eff} and 28 for the highest. In the bottom panel of the figure, the grid is shown in the form of T_m and $\log g$ for our usual choice of $K_m = 1.20$. The simulation points in this figure have the same labels as in the first one. In both figures, a $1.00 M_{\odot}$ track using our new implementation with $K_m = 1.20$ is shown for reference.

From the plots, it is clear that the morphology of the grid changes. It is also evident that the “movement” of the points depends on the surface parameters of the simulation. This has the profound effect that some of the simulation points switch places in the temperature ordering. As an example, simulation 2 is colder than 3 looking at T_{eff} , but hotter in T_m ; the opposite is the case for 8 and

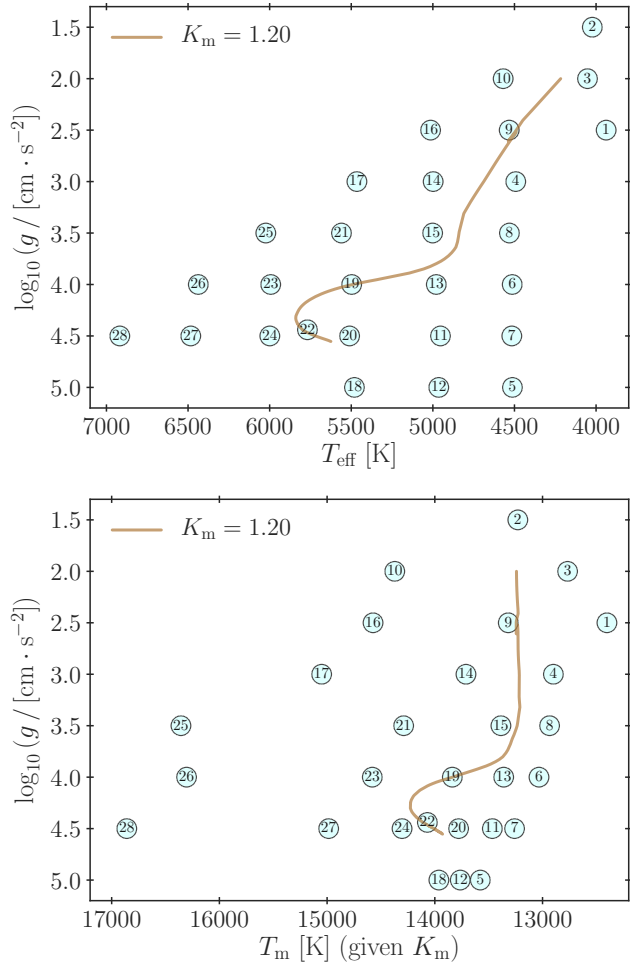


Figure A1. The Stagger grid at solar metallicity. The simulation points are numbered according to T_{eff} . The evolutionary track is for a $1.00 M_{\odot}$ star using (3D)-envelope on-the-fly. *Top panel:* Kiel diagram with the Stagger grid at solar metallicity. *Bottom panel:* Temperature at the matching point, T_m , for $K_m = 1.20$.

6, where the former has the highest T_{eff} , but the latter highest T_m . Another trend is the tendency for the cold simulations to “clump”, which is very evident looking at [5, 12, 18] or [7, 11]. On the other hand, simulations like [3, 10] or [9, 16] instead move away from each other.

These changes in the temperature ordering can affect the triangulation, thus altering the interpolation results; thus, this is directly linked to the observed kinks in the evolutionary tracks in the Kiel diagram.

This paper has been typeset from a $\text{\TeX}/\text{\LaTeX}$ file prepared by the author.